UNIVERSITY OF TWENTE.

PHYSICS OF FLUIDS

Drop Spreading on Complex Surfaces

June 28, 2013

Author:
B.B.J. Stapelbroek

Graduation committee:
Prof. dr. R.M. van der Meer
Dr. J.H. Snoeijer
Dr. A. Eddi
Dr. E.S. Kooij

UNIVERSITY OF TWENTE

Abstract

Faculty of Science and Technology
Physics of Fluids

Master of Science

Drop spreading on complex surfaces

by Bram Stapelbroek

In this thesis we study how the initial stage of drop spreading is influenced by surface properties. For smooth, homogeneous surfaces the radius of the wetted area was previously found to grow as the square root of time. We report that there is no influence on this $\frac{1}{2}$ power-law by the introduction of micron-sized pillars, chemical heterogeneity or by viscoelasticity of the surface. However at later times, a deviation from the $\frac{1}{2}$ power-law is observed. Despite the different types of complexities of the substrates, our results show that this deviation is universal and that data for different substrates can be collapsed when the cross-over times are synchronized. The cross-over time is found to depend on the equilibrium contact angle only, in contrast to previous work that suggested a different spreading exponent for each contact angle.

Contents

Chapter 1

Introduction

In nature and everyday life, interactions between drops and surfaces can be found everywhere. Most common are of course raindrops impacting on a surface. These drops impact on a wide variety of surfaces and the physics involved can be totally different if the surface has other properties. We can think of raindrops that fall on soil, on a car, in pools, on certain plants or on skin. In physics, these examples are referred to as drops that impact on sand, on smooth hard surfaces, on a fluid layer, on structured surfaces or on soft surfaces. These are just a few examples of the variety of drop-surface interactions, which all have their own impact and spreading dynamics.

From industry, there is much interest in the physics of drop-surface interactions because of the wide range of applications where these occurs. For example, in spray painting/cooling, inkjet printing and in internal combustion engines, but also in agriculture, coatings and car tires [1]. There exist many parameters that influence these processes like impact velocity, surface temperature [2] and surface properties. To focus on the interaction between the drop and surface, we will only consider drops gently brought into contact with a substrate, removing the effect of initial kinetic energy of the impacting drop. After contact is established, the drop will rapidly spread. Such spreading and wetting phenomena are relevant in soldering, coalescence, high tech microfluidic devices and much more [3], [4]. Here we will address how this spreading is affected by complex surfaces.

1.1 Static drops

One of the best known scientists in wetting is Thomas Young (1773-1829). Young's law states the static equilibrium contact angle can be calculated from the interfacial tensions

between the three different phases (gas/liquid/solid) [5]. It proved to be a revolutionary article because it was built around the interfacial tension between two phases, now better known as the concept of surface tension [6]. Surface tension is the energy per unit area [J/m^2] between two phases, usually between a liquid and a gas and has a microscopic origin. Molecules at the surface don't experience the same force from every direction like molecules in the bulk do [7]. They feel a force of the liquid from one side, and a force of the other phase (gas/solid) from the other side. The difference between these forces results in an increase of the free energy per unit area, this is the interfacial energy which we call surface tension. The units allow for surface tension to be interpreted as a line force [N/m]. Based on the work of Young and the according mathematical description of Laplace, the Young-Laplace equation, describing the pressure in a drop, has been developed. Since then, much more work has been done in the field of wetting and spreading physics. A classical review is given by [8], later also by [9] and [10].

1.2 Spreading drops

The main topic in this thesis is the dynamic process of drop spreading. We would like to answer the question: How does a drop spread over a complex surface? As schematically can be seen in figure 1.1, there are two different geometries encountered during spreading, which correspond to two totally different regimes. In the top figure, the geometry which is related to late times is shown. This has been studied in the late seventies by L.H. Tanner [11]. He investigated the long term spreading behavior of a drop on a perfectly wetting, smooth surface and found that the radius of the wetted area scales with $t^{\frac{1}{10}}$. This scaling follows from a balance between viscous forces and surface tension: When the liquid is perfectly wetting the substrate, the surface tension forces drive the flow, resisted by the viscous friction in the liquid. This late-time regime is well established and will not be in the scope of this research.

In the bottom part of figure 1.1, the geometry corresponding to the initial phase of the same drop on the same surface is shown. Here the capillary forces are strong, as can be seen by the high curvature of the fluid surface. This curvature induces a large pressure following Young-Laplace's equation and leads to rapid movement of the contact line. In the case of water, which is a low-viscosity fluid, the regime lasts only for a few milliseconds. Therefore, only recently scientists have been able to investigate this regime more closely with the help of high-speed cameras.

Biance *et al.* showed that for water drops spreading on a smooth, perfectly wetting surface, inertia limits the spreading in the initial regime instead of viscosity [12]. Leading to the name inertial regime, where the radius of the wetted area scales with $t^{\frac{1}{2}}$. This
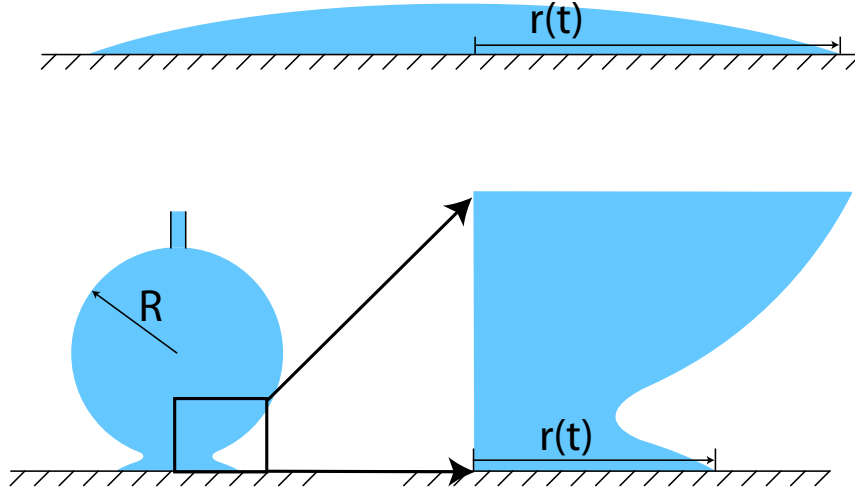
FIGURE 1.1: Different stages of drop spreading exhibit very different geometries. At the late stage, Tanner's law $r \sim t^{\frac{1}{10}}$ is dominant (top), while in the early stage the dynamics follow $r \sim t^{\frac{1}{2}}$ (bottom).

power-law in the inertial regime, was predicted by Eggers in analogy with two coalescing inviscid drops [13].

Surfaces where the drop has a finite contact angle θ, in its equilibrium position, are called partially wetting surfaces. The influence of these partially wetting surfaces on the spreading of millimetric sized water drops has been studied by Bird *et al.* [14]. They argue the equilibrium contact angle modifies the exponent of the power-law: $r \sim t^{\alpha(\theta)}$. Finding a $\frac{1}{2}$ exponent on a perfectly wetting surface and a $\frac{1}{4}$ exponent on a partially wetting surface for equilibrium contact angles of respectively 3° and 117°.

An overview of all recent work on the initial phase of drop spreading is given in figure 1.2 from [10]. The graph on the right includes the more extensive work on initial spreading dynamics by [15] in the Physics of Fluids group and the work from [12] and [14]. The snapshots on the left are side view images from [14], in which the difference between spreading on surfaces with different contact angles can be observed. By introducing a bottom view camera, Winkels *et al.* extend the $\frac{1}{2}$ power-law to ~ 1 μs after contact between the surface and the drop. Looking at these very early times, a collapse for every wettability in the experiments is shown. It remains unclear however, how this collapse to the $\frac{1}{2}$ power-law relates to the interpretation by Bird *et al.* of an exponent $\alpha(\theta)$ that depends on the contact angle θ. Also it remains to be investigated when the transition from the $\frac{1}{2}$ power-law to the equilibrium contact radius for partially wetting surfaces takes place.
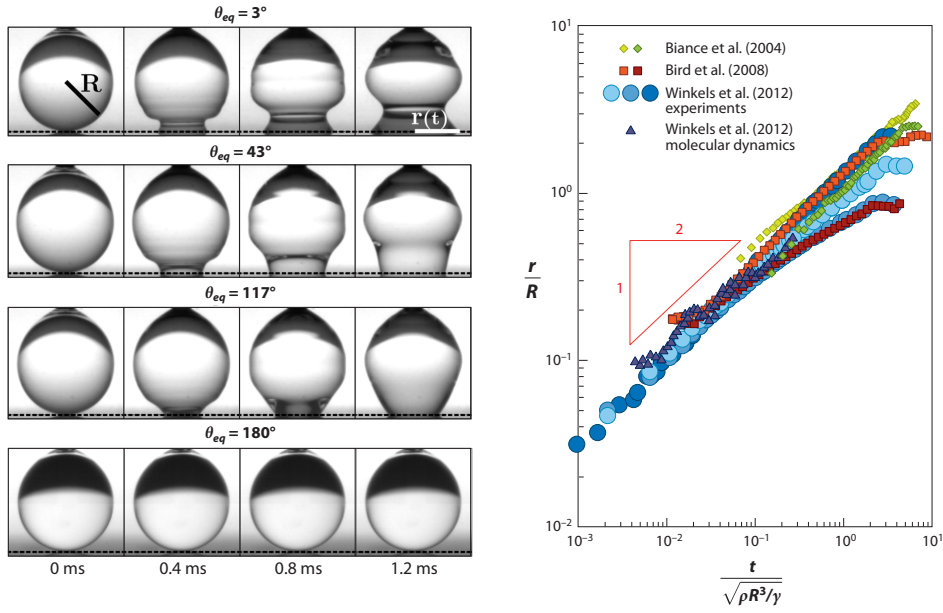
FIGURE 1.2: Figure from [10]. (a) Inertial spreading on surfaces with different contact angles, R = 0.82 mm, [14]. (b) Double logarithmic non-dimensional plot of the contact radius as function of time for perfect and partially wetting smooth surfaces. The $\frac{1}{2}$ scaling exponent is represented by the red triangle. Data from [12],[14],[15].

1.3 Surfaces parameters

All the spreading phenomena discussed so far are based on theory and experiments regarding a hard smooth surface with constant wettability. However, the effect of other parameters, like surface roughness and liquid properties, on the spreading of a drop, should be investigated for a complete understanding. Some experiments have recently been done where liquid properties are varied [16]. For surface parameters, complex surfaces like micro-structured surfaces with pillars or chemically striped surfaces lead to exotic spreading behavior, resulting in square 1.3(a) or elongated 1.3(b) shapes [17],[18] at late times.

The introduction of a "soft" surface can also be interesting. It is known it influences capillarity phenomena like evaporation [19], due to elastic deformation of the surface [20]. So how does such a soft surface influence the spreading behavior?

In this thesis we will focus on the initial spreading behavior of a drop on three types of complex surfaces:

- Structured surfaces (micrometer-sized pillars)

- Chemically heterogeneous surfaces (alternating hydrophobic and hydrophilic stripes)

- Soft surfaces (elastic deformation)
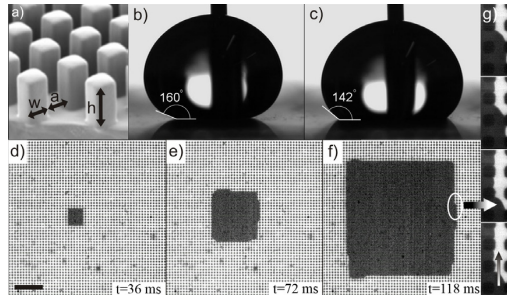
(a) Figure from [17].
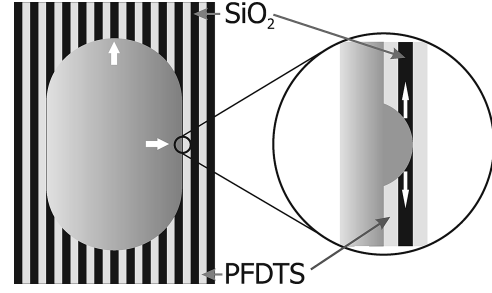
(b) Figure from [18].

FIGURE 1.3: (a) Spreading on micropillars can lead to a square wetted area due to zipping. (b) Spreading on a heterogeneous surface can give an elongated drop shape.

With the use of a combined bottom and side view camera, experiments are done to investigate the spreading for very early times after the start of the process. After analyzing, the results will give us insight in the spreading behavior of drops on complex surfaces.

We will start by giving some more detailed background about spreading in Chapter 2, extra attention will be given to the properties and work done on complex surfaces. In Chapter 3, we will first present the experimental setup used to perform the experiments and then present the preparation and properties of the complex surfaces that we used. This chapter will end with explaining how the measurements are processed. Chapter 4 will start with an example of the results to show how they can be represented, followed by the results from the measurements on the various substrates. In the last chapter, Chapter 5, the findings from the results are summarized and discussed, providing an answer to our initial question: how does a drop spread on complex surfaces.

Chapter 2

Background

Much about the spreading of a droplet on smooth surfaces is already known. We will first present some results for statics and then continue with the dynamics, as we are interested in the very first regime of drop spreading. Some previous theory about this regime is explained and the key results are reviewed. We also provide a short explanation on non-dimensionalization. Finally, some background about the properties of different surfaces is given.

2.1 Young's law and equilibrium contact angle

For small drops, the contact angle is the most important parameter for the shape of the drop, figure 2.1. Therefore, for a given drop volume, it determines the final (equilibrium) radius of the wetted area. It can be calculated from the interfacial energies between the different interfaces. These are denoted as: γ_{sl} for the liquid-solid interface, γ_{sg} for the solid-gas interface and γ_{lg} for the liquid-gas interface. In the case of the liquid-gas interface, γ_{lg} is commonly known as the surface tension of the liquid. Balancing these interfacial energies around the contact line gives, [5]

$$\gamma_{lg} \cdot \cos(\theta_{eq}) = \gamma_{sg} - \gamma_{sl}, \tag{2.1}$$

Where θ_{eq} is the equilibrium contact angle of the surface. In the specific case where $\gamma_{lg} < \gamma_{sg} - \gamma_{sl}$, it follows from equationi 2.1 that $\cos(\theta_{eq}) > 1$ in which case the drop cannot obtain a finite angle. This is the regime where a drop will spread indefinitely, also referred to as complete wetting ($\theta_{eq} = 0°$).
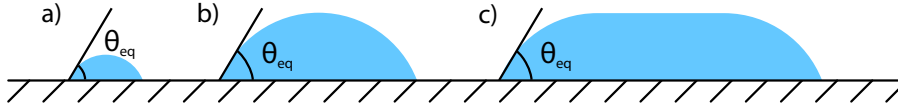
FIGURE 2.1: The contact angle θ_{eq} of a drop is given by the properties of the three phases and is independent of the size of the drop. a) A small drop, forming a spherical cap. b) A larger drop, still smaller than the capillary length, having a spherical shape. c) A drop larger than the capillary length, gravity deforms the shape but θ_{eq} is still the same.

A drop is considered small when gravity forces are negligible compared to capillary length, given by: $l_{cap} = \sqrt{\frac{\gamma}{\rho \cdot g}}$. If the drop radius is smaller than this length, the drop is forced to be a spherical cap [figure 2.1 (a) and (b)]. If it is larger than the capillary length, gravity flattens the drop [figure 2.1(c)]. For all drop sizes, the angle between the drop and the horizontal is determined by minimization of the interfacial energies, resulting in the equilibrium contact angle θ_{eq} according to Young's law. For water, the capillary length is $l_{cap} = 2.7 \cdot 10^{-3}$ m, the drop in the experiments has a typical initial radius of $R = 5 \cdot 10^{-4}$ m, meaning the capillary forces are dominant and the drop has a spherical cap shape at equilibrium. The final radius of the wetted area is thus governed by the equilibrium contact angle.

2.2   Initial spreading

At the moment the drop touches the surface, a singularity arises at the point where the drop is in contact with the surface. The curvature (κ) of the drop at this point goes to infinity as r goes to zero (figure 2.2). This leads to a violent motion of the contact line. In the case of a drop of non-viscous liquid like water, inertia balances this driving force, setting the dynamics of the spreading [12]. Meaning the initial spreading is inertia dominated, the mass of the fluid cannot move to its new equilibrium position any faster.

As shown by previous work [12], a universal power-law with exponent $\frac{1}{2}$ is expected for initial spreading on a smooth surface. This results from a balance between capillary and inertial forces. Rather than balancing the forces, the dynamics of spreading can also be derived from a balance between capillary and inertial pressures. Dimensional analysis shows this as follows.

From geometry (figure 2.2), the curvature of the interface is given by
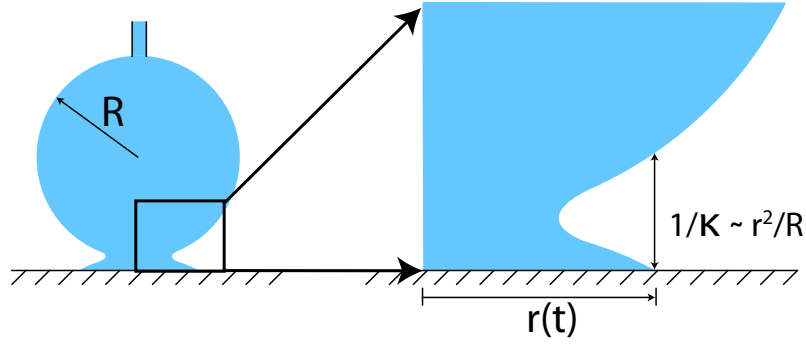
$$\kappa \sim \frac{R}{r^2}, \tag{2.2}$$

FIGURE 2.2: The curvature κ is derived from geometry. The edge of the initial drop can be estimated as $R^2 = x^2 + (y - R)^2$ with the origin at the bottom of the drop. At $x = r(t)$, and for $y = 1/\kappa$, this gives a radius of $1/\kappa \approx r^2/R$

where κ is the curvature, R the initial drop radius and r the radius of the wetted area. This curvature induces a Laplace pressure, $P_{Laplace}$, which is the driving pressure of the spreading. The Laplace pressure is given by the surface tension times the curvature (one over the radius of curvature) and scales as

$$P_{Laplace} \sim \frac{\gamma R}{r^2}. \tag{2.3}$$

This pressure drives the flow to the contact line and is balanced by an inertial pressure which is the resisting force. Inertial pressure is defined through Bernoulli's equation and is written as $P_{Inertial} = \rho \cdot v^2$. In this experiment, the moving contact line speed is the relevant velocity. It can be expressed as a derivative of the radius in time, $v = \frac{dr}{dt}$. From dimensional analysis, we approximate $v = \frac{dr}{dt} \approx \frac{r}{t}$. Balancing the pressures now gives

$$P_{Laplace} \sim P_{Inertial}, \tag{2.4}$$

$$\frac{\gamma \cdot R}{r^2} \sim \frac{\rho \cdot r^2}{t^2}. \tag{2.5}$$

This finally gives

$$r \sim \left(\frac{\gamma R}{\rho}\right)^{\frac{1}{4}} t^{\frac{1}{2}}. \tag{2.6}$$

Meaning r grows as t^α where $\alpha = \frac{1}{2}$. This approach is in analogy with the derivation of the scaling law proposed by Eggers *et al.* [13] for the coalescence of two spherical drops.
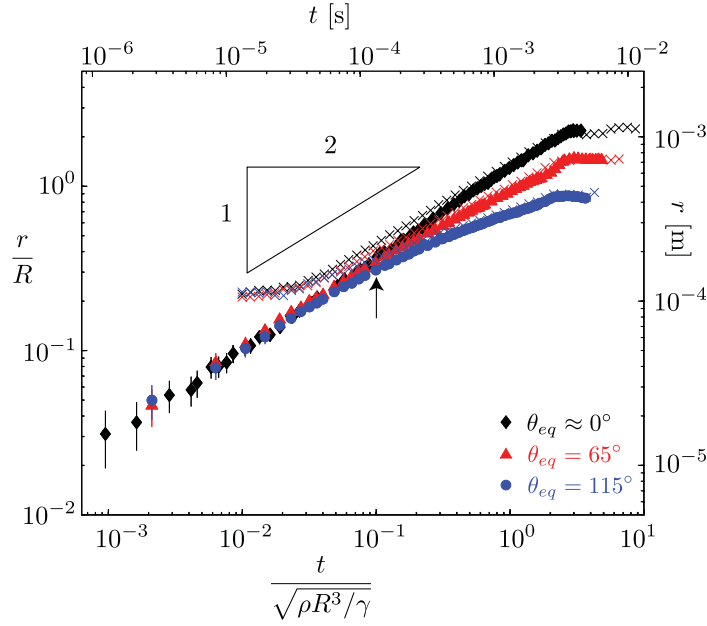
FIGURE 2.3: Figure from [15]. Power-law behavior for three wettabilities. The $\frac{1}{2}$ exponent is shown in the black triangle. All wettabilities follow this behavior in the early stage. Data from [14] is included as crosses, contact angles are $\theta = 3°$, $\theta = 43°$ and $\theta = 117°$. The horizontal preamble is clearly visible for the crosses at $\frac{t}{\sqrt{\rho R^3/\gamma}} \approx 10^{-2}$.

.

We can understand this if we consider the surface as a mirror plane for the flow, this gives the exact same situation as for coalescence and thus the same physics.

As can be seen in figure 2.3, this scaling proposed by [12], has been confirmed experimentally by several groups for perfectly wetting surfaces, [14] and [15]. From the figure it can also be seen why the use of a bottom view camera is necessary when investigating the initial regime of drop spreading. The crosses which correspond to the data from [14], are obtained with a side view camera and show a horizontal pre-amble. With the bottom view data from [15], it is shown that this pre-amble is an artifact of the side view. They also show there is a $\frac{1}{2}$ power-law in the early stage of the spreading for all wettabilities. Only at later times, the partially wetting surfaces show a deviation from this power-law. This is different from the interpretation by [14], where an exponent which is dependent on the contact angle is suggested for the later stage of inertial spreading. Because of the much beter resolution of the data from [15] due to the use of a bottom view camera, this data will be used as a reference for the experimental data obtained in this study.

2.2.1 Non-dimensionalization

In physics, especially in fluid mechanics, a very common tool to compare different measurements, is non-dimensionalization of datasets. The tool enables us to extend specific

measurements, in which the parameters are slightly different, to a more general case in non-dimensional units. In our case, we study the radius of the wetted area, r, as a function of time t. To non-dimensionalize the radius, it has to be divided by a length scale. Here, the natural length scale that influences the radius is the initial size of the drop. Therefore the radius can be non-dimensionalized by dividing it by the radius of the initial drop, R. To non-dimensionalize the time, it has to be divided by a characteristic time, which isn't directly present in the experiment. However, a characteristic time can be constructed using the relevant parameters in the experiment. Combining the initial radius $R \sim [m]$, density $\rho \sim [\frac{kg}{m^3}]$ and surface tension $\gamma \sim [\frac{s^2}{kg}]$ gives an expression with dimension time

$$t_c = \sqrt{\frac{\rho R^3}{\gamma}} \sim [s].$$ (2.7)

t_c is also referred to as the 'capillary time', because it is the only way these parameters can be combined to form a group with the dimension of time. If we now look back at equation 2.6, we divide both sides by the initial radius R, giving us the non-dimensional variables $\frac{r}{R}$ and $\frac{t}{t_c}$ explicitly

$$\frac{r}{R} \sim \left(\frac{t}{t_c}\right)^{1/2}.$$ (2.8)

2.3 Complex surfaces

The physics mentioned above is for the particular case where the surface is smooth and has a constant wettability. Usually surfaces are more complex, they can have roughness or chemical defects that can have a strong influence on the motion of the contact line. In this study we want to find what is the influence of these surface parameters on the spreading of a drop. Therefore we modify the surfaces to mimic some complexities one by one. This is done with accurate control of the surface parameters, making it possible to characterize their influence.

We control roughness by micropillars on the surface. As mentioned in the introduction, we know from literature this can have a major effect on the spreading and the wettability of a surface [21]. It can even cause exotic behavior like Fakir drops [22],[23]. There are two typical situations for a drop on a surface with micropillars, see figure 2.4:
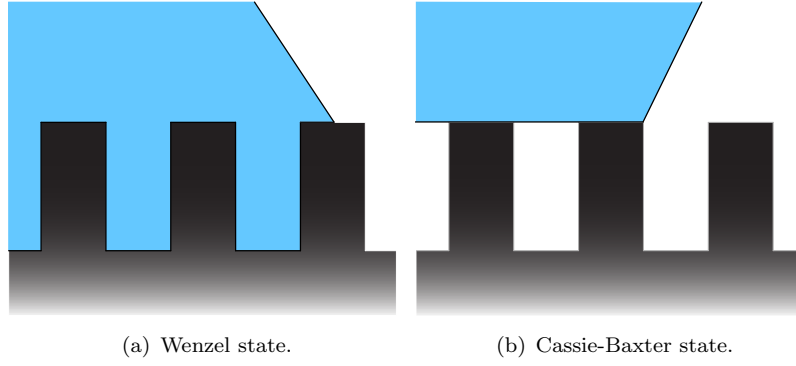
(a) Wenzel state. (b) Cassie-Baxter state.

FIGURE 2.4: (a) A drop in the Wenzel state, filling the space between the pillars. (b) A drop in the Cassie-Baxter state, creating air pockets underneath the drop.

- The Wenzel state, if the pillared surface is hydrophilic, θ_{eq}<90°, the surface will become more hydrophilic. This will cause the drop to fill the space between the pillars, figure 2.4(a)

- The Cassie-Baxter state, if the surface is hydrophobic, θ_{eq}>90°, the surface becomes more hydrophobic. In that case, air pockets are created between the pillars underneath the drop, figure 2.4(b).

The equilibrium contact angle on a rough surface is characterized by the Wenzel relation [24]:

$$cos\ \theta^{\star} = r \cdot cos\ \theta_{eq} \tag{2.9}$$

Where r is defined as $r = \frac{\text{real surface area}}{\text{apparent surface area}}$ and thus is always larger than one for surface roughness. This equation can be used to calculate the equilibrium contact angle of a surface.

A different complexity appears with the introduction of chemical heterogeneity. Such a surface can be obtained by applying a partially wetting coating on a wetting surface [figure 1.3(b)], [25]. The ratio between the width of the hydrophobic stripes and the hydrophilic stripes is defined as β (eq. 2.10). With the Cassie-Baxter equation (eq. 2.11) the equilibrium contact angle in the direction parallel to the stripes, $\theta_{\parallel}$ can be calculated:

$$\beta = \frac{\text{thickness hydrophobic stripes}}{\text{thickness hydrophilic stripes}}, \tag{2.10}$$

$$cos\ \theta_{\parallel} = \left(\frac{\beta}{1+\beta}\right) \cdot cos\ \theta_{eq1} + \left(\frac{1}{1+\beta}\right) \cdot cos\ \theta_{eq2}, \tag{2.11}$$

where θ_{eq1} and θ_{eq2} are the contact angles of the hydrophobic and hydrophilic stripes. The contact angle in the perpendicular direction is governed by the contact angle of the hydrophobic stripes. This is because the drop will spread over the hydrophilic stripe fast and stick on the transition to the hydrophobic stripe. It is only if the real contact angle of the drop becomes equal to the equilibrium contact angle on the hydrophobic stripe that it will cross the transition and wet the next stripe. The influence of other parameters like drop size and impact velocity on the spreading and final shape of a drop on striped surfaces has been studied by [26].
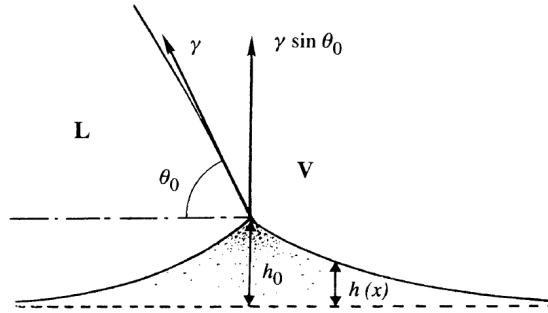

FIGURE 2.5: Schematic representation of the deformation of a soft surface by the contact line. The dotted line is the surface without deformation, θ_0 the equilibrium contact angle, γ the surface tension, h_0 the maximum deformation and $h(x)$ the vertical displacement. Figure from [20].

The last complexity we will investigate is the elasticity of the surface. A surface with an elasticity in the order of gigapascal [GPa] is considered as "hard" and in the order of kilopascal [kPa] or lower is considered "soft". This is related to the deformation of a viscoelastic surface by a contact line [20]. The deformation can be estimated by a simple dimensional argument. The relevant parameters are the force pulling on the surface at the contact line and the elasticity of the surface. Surface tension [N/m] is in this case the relevant parameter for the force, dividing this by the shear modulus G' [N/m^2] results in a length which is the typical height of the deformation. For water on a surface with an elasticity of 10 kPa, this results in a typical deformation of ~ 7 μm, on a surface with an elasticity of 1 GPa, this deformation is just $\sim 7 \cdot 10^{-2}$ nm, which is negligible.

It has been shown recently that there are three regimes of motion for advancing liquid contact lines on viscoelastic surfaces [27]. The high initial spreading velocity represents a high probing frequency of the viscoelastic surface, when the spreading velocity decreases, also the probing frequency decreases [28]. The elasticity is dependent on the probing frequency such that the surface is hard for the early times and becomes softer as the spreading velocity and thus the probing frequency decreases, with three different regimes as a result. In Appendix A there is some more detailed information about the frequency dependent elasticity.

Spreading experiments in the early time regime on soft surfaces have been done by Chen, [29]. The data for the spreading dynamics, $r(t)$, was measured similar to the data in 2.3. The result of these measurements for different $|G|$ is shown in figure 2.6. What is interesting is that the fitted exponent in the early stage of the inertial regime is $\alpha = 0.28$, instead of $\frac{1}{2}$. Recently, spreading for different $|G|$ is studied more extensively, [30]. Here the time of deviation from a fitted power-law $\alpha = 0.3$, was found to decrease for softer substrates. This was interpreted as the onset of a viscoelastic regime. Whether and how this relates to measurements on a rigid surface, remain to be explained.
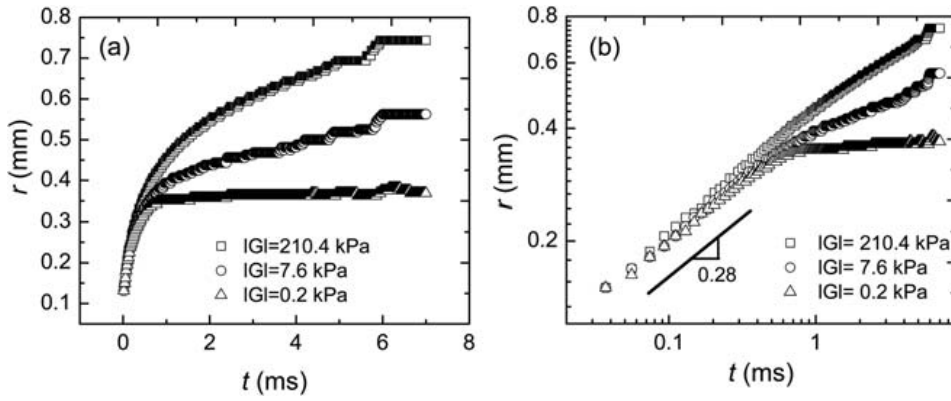

FIGURE 2.6: The spreading of a drop on surfaces with different shear modulus $|G|$ in lin-lin, (left) and log-log, (right) representation. An initial $\alpha = 0.28$ power-law is observed for all $|G|$. Figure from [29]

Chapter 3

Experimental Aspects

3.1 Imaging setup

To study the spreading of a droplet, we need a setup where the important parameters can be controlled and the spreading can be measured. To produce the drop we use a needle and syringe pump. The phenomenon is measured optically, using adapted cameras and illumination sources. Because the produced drop is small, lenses have to be included in the optical system to obtain a magnification that provides an adequate resolution. The setup which is schematically represented in figure 3.1, contains these components.

The needle is mounted at a fixed distance of about 1 mm above the surface, this automatically sets the maximum diameter of the droplet equal to this distance. Ultra-pure Milli-Q water ($\sigma = 0.072 N/m$) is pumped through the needle with a *Harvard PicoPlus* syringe pump, creating a pending droplet. The needle is a *Nordson EFD Precision Tip* with an inner diameter of 0.10 mm and an outer diameter of 0.24 mm. Liquid is being pumped through the needle to inflate the droplet at a rate of 0.001 ml/min until the drop touches the surface and starts to spread. Due to the low flow rate, the approach velocity of the drop is very small (~ 20 μm/s) and is neglected. Because of this low approach velocity and the high intensity light illuminating the droplet, some liquid is evaporated and condenses on the substrate. This only happens in case the humidity of the atmosphere is high. To prevent this, in all cases a cap is placed over the substrate and dry nitrogen gas is pumped into this chamber lowering the humidity and preventing condensation on the surface.

To capture the initial stage of spreading, the surface is placed on a microscope, which has a translational stage. In the experiments, a two camera setup is used. The *Photron SA 1.1* is used to record the bottom view and the *Photron APX-RS* is used to record
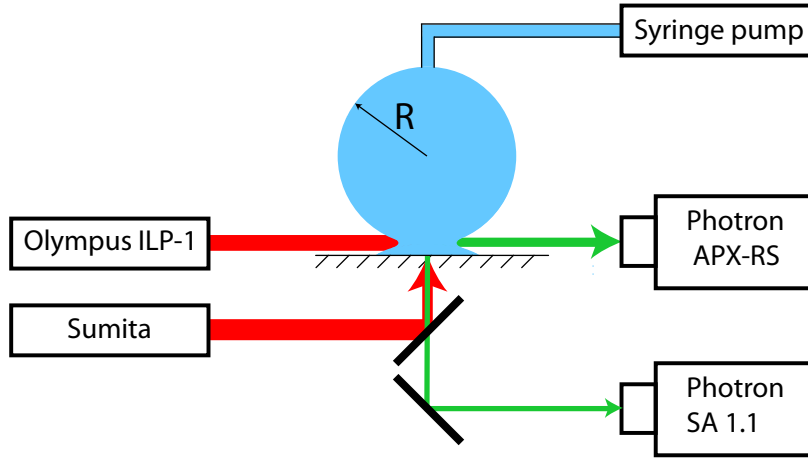
FIGURE 3.1: Schematic overview of the setup and light beams.

the side view. Snapshots of a typical movie recorded with these cameras are shown in figure 3.2. When viewing from the bottom, where the surface is dry the light is reflected. The area where the drop is wetting the surface can be seen as a dark spot, because the contact with the water enables more light to go through, leaving the system.

As shown by [16], using a bottom view camera enables us to examine the early times of the spreading process much better. One can imagine this when looking at the snapshots in figure 3.2. With the *Photron SA 1.1*, recordings at 200,000 frames/s are made. The maximum shutter time is determined by the frame rate as $\frac{1}{\text{fps}}$ s and is thus very short, reducing the light yield. On top of this, the light has to travel from the light source through a beam splitter, then reflects on the surface of the sample and goes back through the beam splitter, to the camera, see figure 3.1. Reducing the intensity of the light by a factor 4 due to the beam splitter alone. To improve the light yield, the high intensity *Sumita* light source is used. With the high illumination intensity we are able to use a $10\times$ magnification objective and a magnification doubler to increase the resolution. This results in a resolution of 2 μm per pixel at 200,000 frames/s. This resolution in time and space is really remarkable.

With the *Photron APX-RS* the side view is captured. An *Olympus ILP-1* light source is used for illumination of the side view, again see figure 3.1. It is triggered by the bottom view camera so the movies can be synchronized. From the side view images, the initial drop size can accurately be determined and the late stage of the inertial spreading regime is captured. Enabling us to adapt the bottom view camera for capturing the very first times. In the intermediate region where both views can be accurately analyzed, they are used to confirm each other. The side view is recorded with a frame rate of 10,000 or 20,000 frames/s, depending on the measurement. For the side view, a long working distance microscope is used to magnify the phenomenon so it can be analyzed
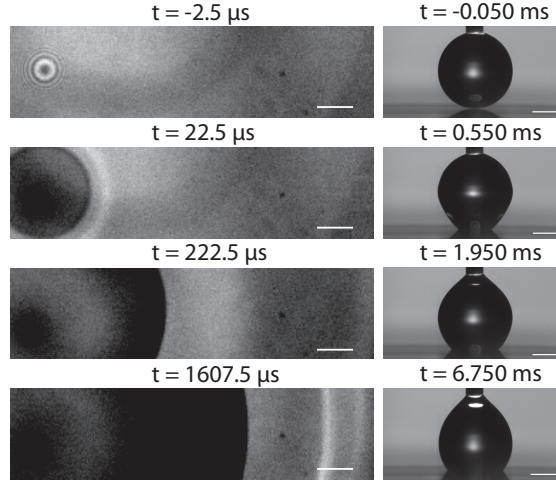
FIGURE 3.2: Snapshots of the bottom and side view at different times. The surface is made of PDMS with standard recipe, has a thickness of 80 μm and elasticity of G' = 1.1 MPa. Length of the bar is 50 μm in the bottom view and 300 μm in the side view recordings. The fringes in the first recording of the bottom view are due to the reflection of the drop pending just above the surface. The grayscale values of the bottom view images are normalized to increase the contrast.

more precisely. After focusing, the magnification can be adjusted without losing the focus, this allows for optimizing the magnification for each experiment. In practice, the magnification is set to a value that suffices to do all the measurements of one day. The resolution is around 3 μm per pixel, but when extracting the data from the images, a precise resolution is determined and implemented for each setting.

3.2 Substrates

In this thesis, we study the influence of the surface properties on the spreading of a droplet. The investigated samples can be divided in three groups based on their characteristics. We used samples with:

- Structured surfaces (micrometer-sized pillars)

- Chemically heterogeneous surfaces (alternating hydrophobic and hydrophilic stripes)

- Soft surfaces (elastic deformation)

In the following subsections, the exact characteristics of each group are given, as well as the substrate preparation techniques.

3.2.1 Structured surfaces

The structured surfaces that are used are glass slides with micropillars. The density and size of these micropillars are a measure for the roughness of the sample and are varied. The microstructures were fabricated with standard photolithography and etching techniques. A Piranha solution (H_2SO_4/H_2O_2) cleaning process is applied to make sure the samples are clean and have a high wettability, a low contact angle, $\theta_{eq} < 5\,°$. This guarantees the drops enter the space between the pillars and achieve a Wenzel state.

The glass substrates with these structured surfaces have square arrays of 5 μm high (H) cylindrical pillars. A schematic is shown in figure 3.3(a) and a SEM image is shown in 3.3(b). The substrate with the most dense distribution of pillars has a separation between the pillars of 5 μm (S) and a pillar diameter of 10 μm (W). For the substrate with the least dense distribution the separation is 40 μm and the diameter is 20 μm. In total, measurements have been done at six different pillar densities.
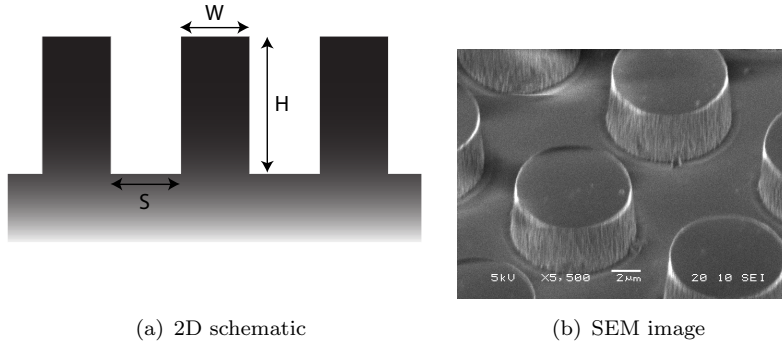

(a) 2D schematic

(b) SEM image

FIGURE 3.3: (a) 2D schematic of the micropillars and the definition of the substrate dimensions: separation (S), diameter (W) and height (H). (b) SEM image of the structured surface, by Rik Groenen.

3.2.2 Chemically striped surfaces

The chemically striped substrates consist of glass with alternating hydrophobic and hydrophilic stripes on the surface. Their respective contact angles are $\theta_{eq} = 110°$ and $\theta_{eq} = 40°$. These are created using self-assembling perfluordecyltrichlorosilane (PFDTS, ABCR Germany) monolayers [25]. The width of the hydrophobic stripes is constant and is 10 μm, the width of the hydrophilic stripes varies between 2 μm and 30 μm leading to ratios from $\beta = 5$ to $\beta = 0.33$, see equation 2.10. In this work, on a striped surface, we distinguish between parallel and perpendicular directions of spreading. Spreading along the stripes is what we refer to as parallel spreading. To the spreading in the 90° rotated direction we refer as perpendicular spreading (figure 3.4).
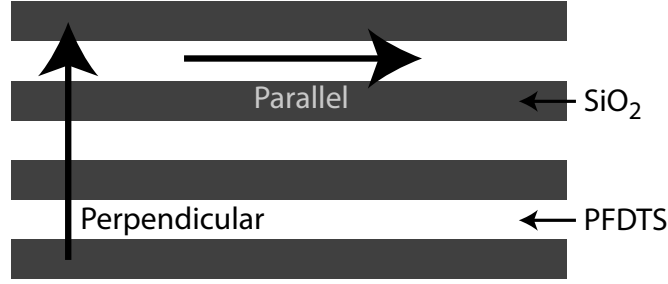
FIGURE 3.4: Alternating wetting and non-wetting stripes. Width of the hydrophobic stripes is 10 μm, the width of the hydrophilic stripes varies from 2 μm to 30 μm. The directions parallel and perpendicular to the stripes are indicated by the arrows.

3.2.3 Soft surfaces

The substrates with a soft surface are made by applying a thin layer of Polydimethyl-siloxane (PDMS) with a film casting knife on a glass slide. The initial thickness of the layer is varied between 50 μm and 800 μm. A sample thicker than 2,000 μm is made by drop casting the oligomer in a glass petry dish. The elasticity of the PDMS is varied by using three different mass ratio's 1:10, 1:30 and 1:50, between cross-linker (curing agent) and pre-polymer (base), resulting in a shear elasticity of: $G' = 1.1$ Mpa, $G' = 41$ kPa and $G' = 32$ kPa at 1 Hz. This is in reasonable agreement with the values in [29] and [19], which are $|G| = 510$ kPa, $|G| = 20$ kPa and $|G| = 7.6$ kPa respectively. For more information on the measurement of G', see Appendix A.

After curing for one hour at $100\,^{\circ}C$, the samples are washed in Tetrahydrofuran (THF, C_4H_8O) to dissolve the un-cross-linked polymer chains. This is necessary because the un-cross-linked polymer chains diffuse to the surface and would influence the elasticity at the surface. The samples with $G' = 1.1$ MPa are not washed, they are made with the recommended amount of cross-linker so no free chains are available. By removing the un-cross-linked chains, the elasticity and surface properties can be better controlled and characterized. The whole washing procedure takes 10 days, mainly because the un-cross-linked polymer chains are only slowly dissolved. First, the samples are put into a bath of THF where they remain for a few minutes to dissolve the free chains at the surface. After this step, the THF-bath is emptied, refilled and closed. This is done two more times with three or four days in between. After the last refreshing of the bath, the THF is slowly evaporated. If the evaporation goes too fast, it could leave cracks in the PDMS surface (figure 3.5). This procedure was advised by the authors of [19]. As a result of the procedure, the thickness of the PDMS layer is reduced, now varying between 13 μm and 215 μm. From the side view recordings, the equilibrium contact angle of the samples is determined. For the PDMS with $G' = 1.1$ MPa we find $\theta_{eq} = 120°$, for $G' = 41$ kPa, $\theta_{eq} = 126°$ and for the surface with $G' = 32$ kPa we find $\theta_{eq} = 136°$.
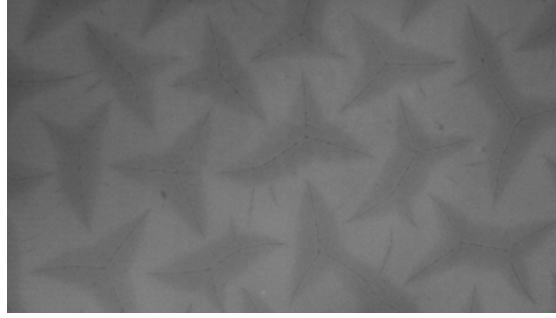
FIGURE 3.5: Bottom view image from the cracks in the G' = 41 kPa samples.

3.3 Image processing

Because the spreading from the center along an axis is assumed to be independent of the direction, only the spreading from the center to one side of the drop is measured. The center is selected manually in one of the first frames after contact.

The movies of the bottom and side view are analyzed to obtain the time evolution of the radius of the wetted area. The radius obtained from the bottom view is used for the times shortly after the drop touches the surface, until one or two milliseconds, depending on the length of the movie. The radius is determined in every frame of the movie by using a convolution technique [31]. An intensity profile is taken from the average of three horizontal lines for which we want to detect the transition from the low-intensity values corresponding to the dark drop, to the high-intensity values corresponding to the surface, see figure 3.6. To prevent detection of other reflections, a region of interest around the radius is analyzed, the intensity in this region is shown in the right half of figure 3.6. Together with a pre-defined function, equation 3.1, in which C is a vector whose length determines the width of the function, the convolution is calculated. The outcome is represented by the red line in figure 3.6.
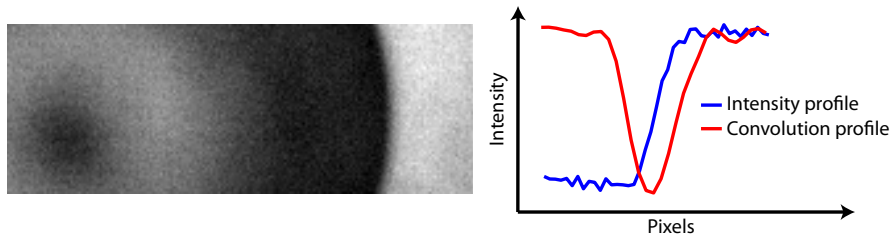
FIGURE 3.6: On the left, a recording from the bottom view. On the right, the averaged intensity profile around the transition from low intensity (dark) to high intensity (bright) is showed by the blue line. The red line is the outcome of the convolution between the intensity profile and function 3.1. Its minimum corresponds to the steepest part of the blue line, which represents the edge of the drop.

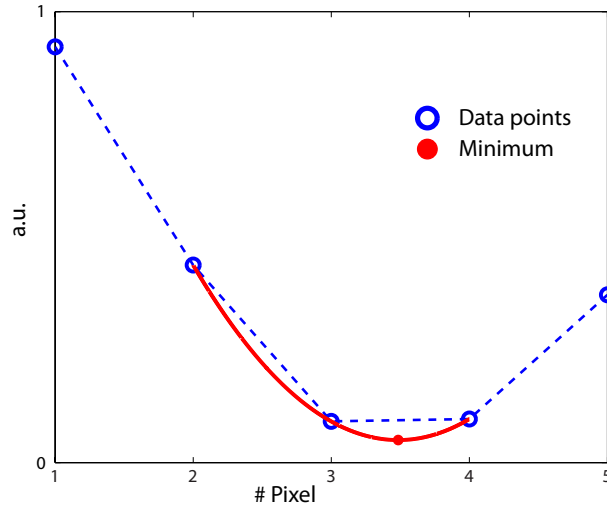$$f = C \cdot e^{-\left(\frac{C^2}{13}\right)} \tag{3.1}$$

FIGURE 3.7: Example of sub-pixel detection. The blue data points correspond to pixel values. The red dot is the minimum of the parabola fitted through the lowest and two surrounding points, giving a sub-pixel resolution of the minimum.

The pre-defined function is defined such that the minimum of the convolution, corresponds to the steepest upward slope of the intensity profile. The edge of the wetted area can now be detected by finding the minimum value of the convolution with sub-pixel detection, see figure 3.7. Sub-pixel detection is done by fitting a parabola through the three points nearest to the minimum. The minimum of this parabola is the sub-pixel minimum of the convolution.

The SA1.1 records the movies in 12bit depth, the greyscale ranges from 0 to 4095. This increases the difference between the high and low intensity pixels, which makes it easier to detect the transition. Because pixels on a monitor are only 8bit, the 12bit depth can be exploited to represent the images with more contrast.

For the analysis of the side view, first the surface is detected to get the intensity profile at the correct height, figure 3.8. Then the same convolution technique is used to detect the edges of the drop. At the interface from the background to the drop we look for the maximum of the convolution outcome because the transition is from high to low intensity, instead of from low to high.
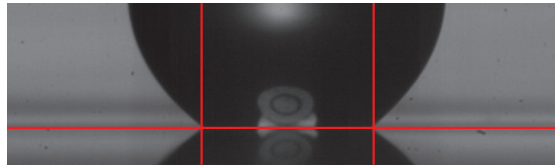

FIGURE 3.8: Recording from the side view with detection of a PDMS surface with G' = 32 kPa. The horizontal line is the detected surface, the vertical lines are the detected edges of the wetted area.

3.3.1 Start and initial frame

As the images are analyzed and the data is extracted, the time evolution of the radius of the wetted area can be plotted. Because we expect a power-law behavior from smooth silica data and the analogy with coalescence [13],[15], the data is best plotted on a double logarithmic scale. The difficulty of such plots is that it requires to determine the initial time with good resolution. There is only a 5 μs difference between the frames, so especially for the data of the first few frames, high accuracy is necessary. This is difficult because there is no possibility to exactly define the beginning of the process. The solution we therefore used, is to define the time exactly between the first frame where contact can be observed and the frame before, as the start of the process. This reduces the error to the half of a period between two frames. These horizontal errorbars are still quite large though, in a log-log plot the left side of the first point even extends for infinity. The initial frame can be found by using Matlab to display the absolute difference in intensity between two consecutive frames. The first frame in which the difference is caused by the drop wetting the surface, is then selected manually.

The times of the side view are synchronized with the times of the bottom view. This is necessary because the length of the recorded and analyzed movies is different for each camera. The error in time from the bottom view is hereby also introduced in the time of the side view, because the side view times are in the order of milliseconds, this error is not large anymore.

Chapter 4

Results

In this chapter we present our experimental results. We will first describe the data obtained for a typical experiment. Then we consider the three different substrates: structured surfaces in section 4.2, chemically striped surfaces in 4.3 and soft surfaces in section 4.4. Finally we will discuss the contact angle dependence observed for the three different types of substrates and provide a collapse of the experimental data in section 4.5.

4.1 Typical experiment

The analysis of the measurements, with all necessary actions, leads to the desired values of the wetted radius r, as function of time. Plotting this data results in figure 4.1 for a perfectly wetting structured surface. The blue points are extracted from the bottom view and the red points are extracted from the side view. In the figure, an image from the bottom view and the side view is included in the top left and bottom left corner respectively.

As already stated in the introduction, we want to compare the spreading on complex surfaces with the spreading observed on smooth silica. From figure 4.1 however, the initial stage is hard to see. As the data ranges over more than three decades, it is much more convenient to plot the data on a log-log scale, shown in figure 4.2. The initial regime can now be seen in full detail. In a log-log plot, a straight line indicates a power-law $r \sim t^{\alpha}$, where the slope of the straight line gives the exponent α. The best fit is obtained for $\alpha = 0.55$.

The figures 4.1 and 4.2 are from a single measurement on a structured surface. To reduce uncertainty, we performed at least 5 measurements per surface. Although the
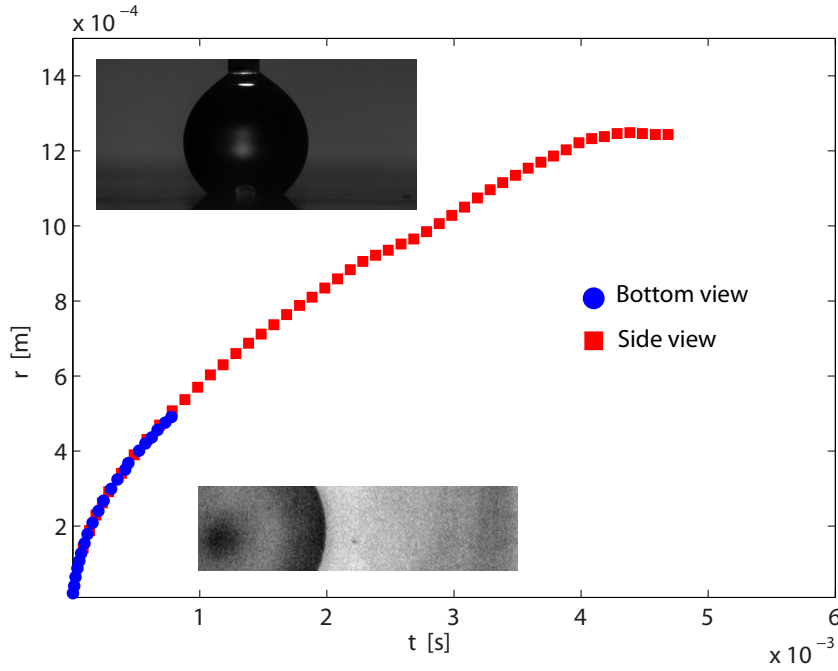
FIGURE 4.1: Development of the wetted radius in time on a perfectly wetting structured surface with a pillar diameter of 20 μm and separation of 10 μm (table 4.1, structure 3). Blue diamonds and red squares are data from the bottom and side view respectively. The insets are typical images from the side and bottom view on a soft surface, respectively in the top left and bottom left corner.

physics is the same, it is inevitable to get slight differences between measurements due to experimental errors. Plotting all five measurements in the same figure can become crowded as multiple surfaces are plotted in the same figure. To cope with this, all measurements on the same surface are averaged and plotted as a single curve with errorbars, see figure 4.3. The errorbars are an indication of the difference between the separate measurements. They are given by the standard deviation and are set to a minimum of two times the pixel size to compensate for analysis errors.

As we are comparing different measurements with slightly different drop radii, we report our results in non-dimensional form, $\mathcal{R}$ as a function of $\mathcal{T}$. Where $\mathcal{R} = \frac{r}{R}$ and $\mathcal{T} = \frac{t}{t_c}$, where t_c is given by equation 2.7. From here on, all plots will have non-dimensional units for this reason.

In figure 4.3, a graph is shown of the average over five measurements on a single surface. The black points are the data points from measurements on perfect wetting smooth silica by Winkels et al. [15] and confirm the analysis results in the same non-dimensional curve. This data will be used as a reference case in some of the following figures.
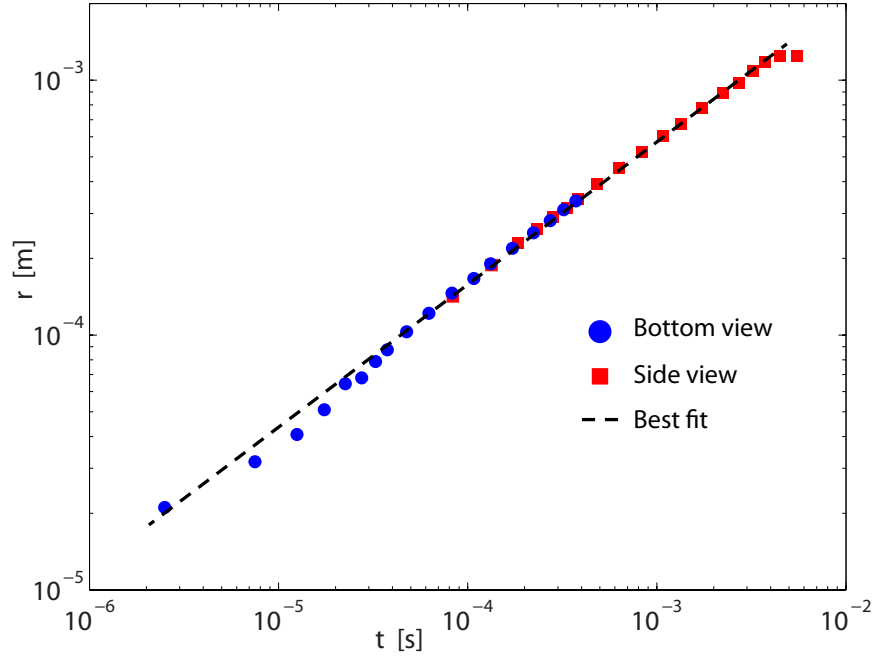
FIGURE 4.2: A single measurement on the same surface as in figure 4.1. Bottom and side view are plotted in a log-log representation. The dashed line indicates the best fit for $\alpha = 0.55$.

FIGURE 4.3: The red dots are an average of five measurements on the same surface as in figure 4.1. The black diamonds are the data points for spreading on smooth silica from [15]. The errorbars indicate the standard deviation of the measurements, the error for the smooth silica data is indicated by the gray area and will be used as reference in the following figures.

4.2 Structured surfaces

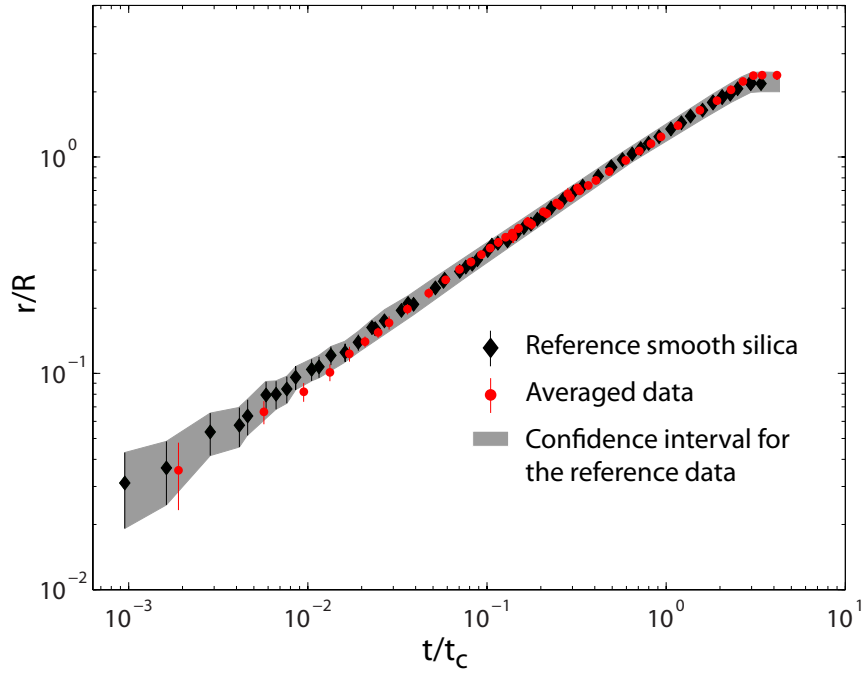We first look into the spreading of drops on a surface with micropillars. The spreading dynamics for 6 different structures with different pillar sizes and spacing (see table 4.1) is shown in figure 4.4. With the combined bottom and side view, we reveal a common regime of spreading behavior over three decades in time: all the datasets collapse on a single curve. This is independent of the pillar size or density. We also see that this regime does not show a significant deviation from the smooth silica reference curve from [15]. The micropillar structure at the surface appears to have no influence on the $\frac{1}{2}$ power-law.
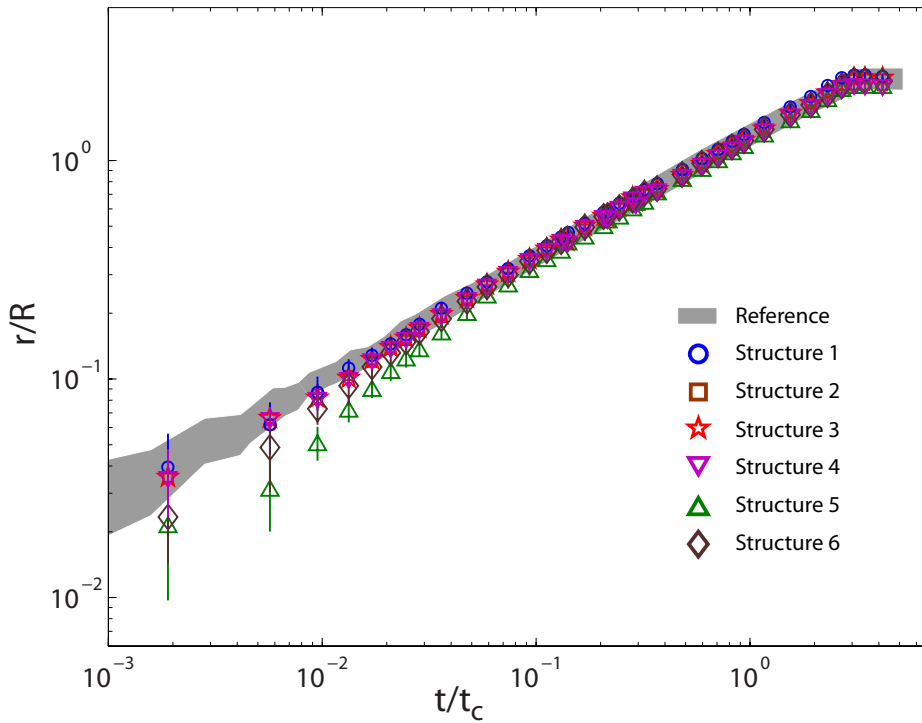
FIGURE 4.4: Non-dimensional wetted radius over time in a log-log graph. The averaged curves of six structured surfaces with different pillar sizes and densities, see table 4.1. For each average, five measurements are done. The gray area indicates the errorbars of the reference curve.

	Height (μm)	Separation (μm)	Width (μm)
Structure 1	5	5	10
Structure 2	5	10	10
Structure 3	5	10	20
Structure 4	5	20	10
Structure 5	5	20	20
Structure 6	5	40	20

TABLE 4.1: Different micropillar sizes and densities.

FIGURE 4.5: Snapshots from the bottom view, the circles are the pillars. On the left, the spreading over the first pillar of a s100 w100 structure can be seen, this structure is only used to illustrate the spreading on the top of the pillar. On the right, the drop immediately spreads over multiple pillars s5 w10. The length of the bar in the right bottom corner is 100 μm.
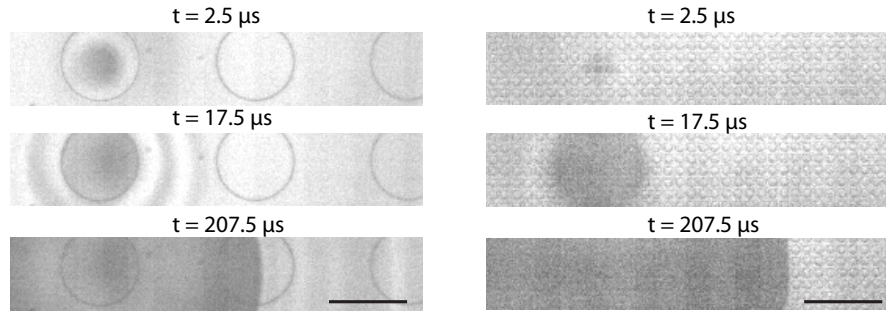
When presenting this data, special attention was given to the initial stage. During the analysis we found out the drop first spreads over the top of a pillar and then has to slide down the pillar (figure 4.5). For small pillar diameters it wets the whole pillar in a single frame (right). For larger pillars, the wetting of the top of the pillar can be observed (left). After the top is wetted, the drop slides down along the sides of the pillars until it touches the bottom of the surface, where the actual spreading we are interested in starts. This complicates the analysis because not only the actual time of contact is harder to identify, there is also a wetted area with a finite radius at the moment the droplet touches the bottom of the surface. The slight initial deviation from the $\frac{1}{2}$ power-law and large magnitude of the errorbars are a result of this and confirm we are really looking at the edge of what we can possibly resolve.

4.3 Chemically striped surfaces

We now consider the spreading on chemically heterogeneous surfaces. As these surfaces have a different ratio β, between the width of the hydrophilic and hydrophobic stripes, the equilibrium contact angle in parallel direction is also different for every surface. $\theta_\parallel$ is given by equation 2.11. $\theta_\perp$ is dependent on the contact angle of the hydrophobic stripes. The absolute width of the stripes is given in table 4.2. For the definitions of the parallel and perpendicular direction, see figure 3.4. Due to the stripes, every striped sample is not axisymmetric but has two symmetry axes in the horizontal plane. We separately determine the spreading along these two axes, looking at the development of the radius of the wetted area along the chosen axis.

β	0.33	0.4	1	2	5
Hydrophobic (μm)	10	10	10	10	10
Hydrophilic (μm)	30	25	10	5	2

TABLE 4.2: Stripe width for given β.

In figure 4.6 the wetting in parallel and perpendicular direction on a surface with $\beta = 0.4$ is shown. The blue squares indicate the spreading in the perpendicular direction. The red circles indicate the spreading in parallel direction. We again see the $\frac{1}{2}$ power-law behavior for the initial phase of the spreading along both axis. This implies the spreading is axisymmetric in the initial stage, despite the anisotropic properties of the surface. When the spreading leaves this power-law, we see it slows down more along the perpendicular than along the parallel axis. This results in a smaller final radius of the drop along the perpendicular axis. The anisotropy of the surface is thus observed during the final stage of the spreading, resulting in an elongated final shape of the drop.
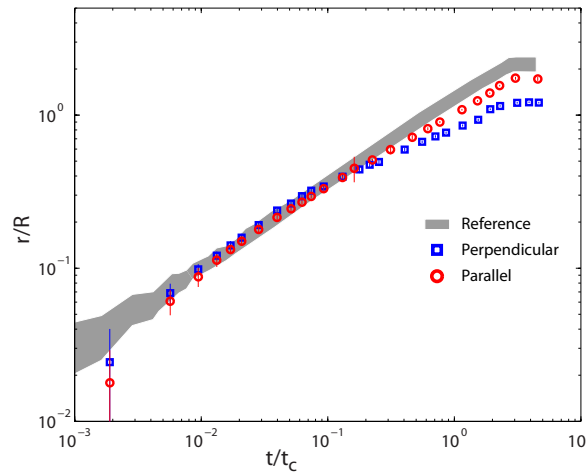

FIGURE 4.6: Chemically striped pattern with $\beta = 0.4$. The difference in final contact radius between the perpendicular and parallel spreading direction can clearly be seen.
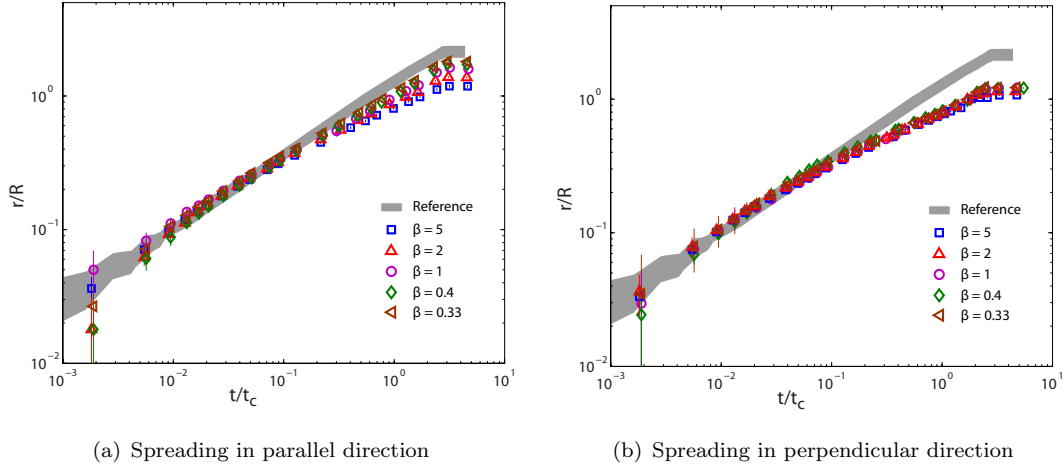
(a) Spreading in parallel direction   (b) Spreading in perpendicular direction

FIGURE 4.7: Spreading behavior of drops on a chemically striped surface. (a) In the parallel direction, β influence the final radius. (b) In the perpendicular direction, the final radius is unaffected by β.
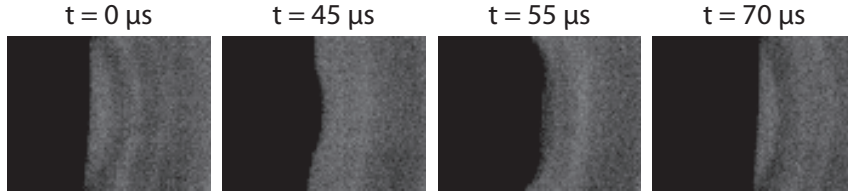

FIGURE 4.8: Four snapshots from the bottom view for a striped surface with $\beta = 1$. For the first still, t is set to zero. The second still is the frame in which the contact line moves over the transition from a hydrophilic to a hydrophobic stripe. The last still is when the contact line is stuck on the next transition.

We see in figure 4.7(a), that the final radius for spreading along the parallel axis increases with decreasing β. This is what we expected because for smaller β more of the surface is hydrophilic. Along the perpendicular axis (figure 4.7(b)), the final radius remains almost constant for decreasing β. From this we infer that the difference in final radius between the parallel and perpendicular direction increases for reducing β, thus the drop becomes more elongated as the hydrophilic stripes become wider. In both direction the initial spreading follows the $\frac{1}{2}$ power-law, and within experimental error this dynamics is identical to that of smooth silica.

In the perpendicular direction, zipping wetting [32], can be observed as a result of the stick-slip motion of the moving contact line, figure 4.8. When the contact angle becomes larger than the equilibrium contact angle on the hydrophobic stripe, the contact line crosses the transition, figure 4.8(b). It spreads over the hydrophobic and hydrophilic surface, figure 4.8(c), until it reaches the next transition from a hydrophilic to hydrophobic stripe, where it sticks again, figure 4.8(a),(d). While it sticks, the spreading in parallel direction of the stripes continues, causing the zipping.

4.4 Soft surfaces

We finally investigate the spreading over soft surfaces, which exhibit elastic deformation. First shown by [33], deformation of the viscoelastic surface by the contact line dissipates energy and therefore might slow down the spreading. In the following we vary the shear modulus G', the contact angle θ and the thickness of the surface layer. For an indication of the size of the deformation, we can divide the surface tension by the shear modulus of the surface. For water on a surface with shear modulus $G' = 72$ kPa, $\frac{\gamma}{G'}$ results in a substantial vertical deformation of approximately 1 μm.

In figure 4.9 we see the results of the measurements on PDMS surfaces with four different thicknesses and a shear modulus of $G' = 32$ kPa. As can be seen in figure 4.9(a), all measurements on the partially wetting PDMS layer fall on top of each other, indicating there is no influence of the thickness of the PDMS layer on the spreading behavior. Further we observe the measurements follow the reference curve for a few points, before the spreading decreases more than the reference and reaches its equilibrium radius. We see the final radius of the wetted area on the PDMS surface is a lot smaller than the radius of the wetted area on the reference surface. This is caused by the high contact angle on the PDMS surface, in contrast to the very small contact angle in the reference case.

In figure 4.9(b), the same surfaces are plasma cleaned to make them perfectly wetting before the experiments are repeated. The result is again that the curves for different surface thicknesses overlap, the thickness does not influence the spreading. In this case,

(a) Partially wetting PDMS, $G' = 32$ kPa (b) Perfectly wetting PDMS, $G' = 32$ kPa
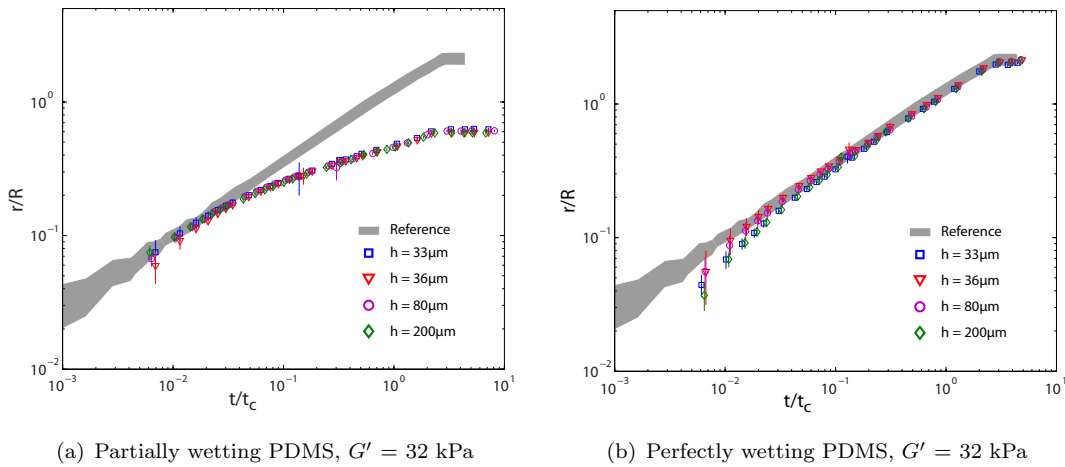
FIGURE 4.9: The spreading of a droplet on a PDMS surface with $G' = 28$ kPa and four different thicknesses. (a) The surface is partially wetting and has an equilibrium contact angle of 136°, all curves fall on top of each other. (b) Same, only the surfaces are plasma cleaned making them perfectly wetting, $\theta_{eq} < 5°$.

the data also overlaps with the reference curve within experimental error. This indicates that the elasticity of the surface is not of importance. When only the wettability is changed such that it is comparable to the reference case on hard smooth silica, the spreading behavior is identical.

The question that now arises is what causes the deviation from the $\frac{1}{2}$ power-law behavior. We have seen the thickness of the PDMS does not influence the spreading. More importantly, when the samples are plasma cleaned to make them perfectly wetting, the spreading is identical to the spreading on perfectly wetting smooth silica surfaces. Indicating there is no influence of the surface properties at all as the surface is perfectly wetting. This independence of the thickness and surface properties also seems to be true for the other PDMS samples with elasticities of $G' = 1.1$ MPa, figure 4.10. Where the data from the plasma cleaned surface with low contact angle is again identical to the reference case, figure 4.10(b). This suggests the deviation must be a consequence of the only parameter remaining, the equilibrium contact angle. The data from the measurements on surfaces with $G' = 41$ kPa are not shown because they are identical to the data for surfaces with $G' = 32$ kPa and $G' = 1.1$ MPa.

The first points after contact are below the reference, this can be explained by the difficult detection of the radius in the first frame. Also in the first frame of a log-log plot, high accuracy is required because all differences are enlarged extremely. Apparently the accuracy we obtain is not sufficient for the first frame. Apart from this first point we do see the $\frac{1}{2}$ power-law in the early stage.

(a) Partially wetting PDMS, $G' = 1.1$ MPa

(b) Perfectly wetting PDMS, $G' = 1.1$ MPa
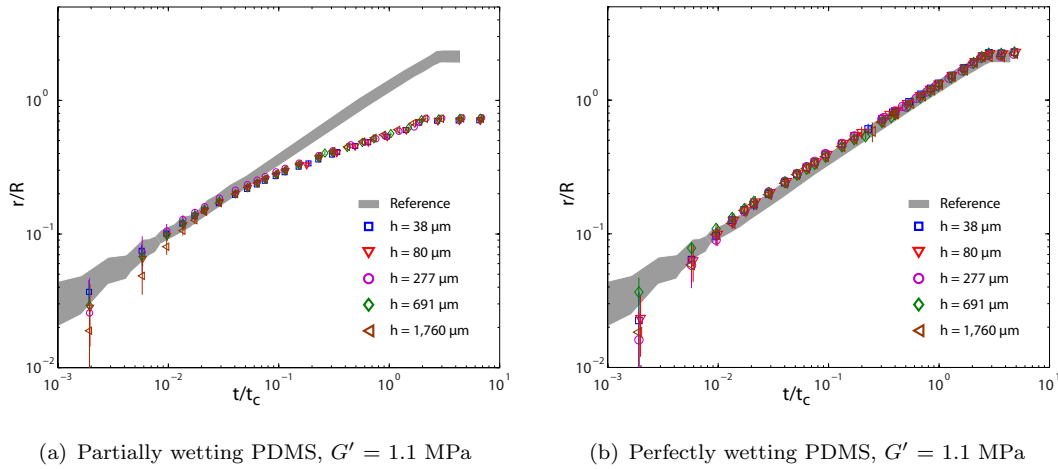
FIGURE 4.10: The spreading of a droplet on a PDMS surface with $G' = 1.1$ MPa and five different thicknesses. (a) The surface is partially wetting and has an equilibrium contact angle of 120°, the curves for different thicknesses are all identical. (b) Same as for the partially wetting surface, only the surfaces are plasma cleaned making them perfectly wetting, $\theta_{eq} < 5°$.

4.5   Contact angle dependence

As the previous results have shown, we see an initial regime where the drop spreads with a $\frac{1}{2}$ power-law for all surfaces, thus also regardless of the contact angle. For the perfectly wetting surfaces this power-law holds even at later times, just as it does for the reference case on smooth silica, [12], [14], [15]. However, we do see a deviation from the reference after a certain time for the partially wetting surfaces. This deviation seems to occur earlier for surfaces with a larger contact angle, independent of other surface parameters. From this, we propose an interpretation where the equilibrium contact angle determines the dynamics of drop spreading.

We try to find a way to determine if the deviation can be explained by the contact angle only. Assume the final radius of the wetted area determined by the contact angle is the only parameter causing the deviation from the $\frac{1}{2}$ power-law. Then there should be a way to collapse the part before the final radius is reached, for all curves. First we introduce once more the non-dimensional forms of the radius, $\mathcal{R} = \frac{r}{R}$ and the time, $\mathcal{T} = \frac{t}{t_c}$. The radius depends on time to the power of one half, times an unknown function dependent on the time and the substrate properties:

$$\mathcal{R} = \mathcal{T}^{\frac{1}{2}} \cdot f(\mathcal{T}, substrate). \tag{4.1}$$

The unknown function $f(\mathcal{T}, substrate)$, goes to a constant as $\mathcal{T}$ goes to zero. This takes place in the universal initial regime where the exponent is $\frac{1}{2}$,

$$\lim_{\mathcal{T} \to 0} f(\mathcal{T}, substrate) = C. \tag{4.2}$$

Since it reduces formula 4.1 to $\mathcal{R} = \mathcal{T}^{\frac{1}{2}} \cdot C$, where C is of order unity from previous experiments [15]. We now hypothesize that f is not a function of all surface properties, but only of the final contact angle θ

$$\mathcal{R} = \mathcal{T}^{\frac{1}{2}} \cdot f\left(\frac{\mathcal{T}}{\tau(\theta)}\right). \tag{4.3}$$

Here, $\tau(\theta)$ is the cross-over time for which the underlying wettability of the substrate is noticed. $\tau(\theta)$ can be found by shifting all curves along the $\frac{1}{2}$ power-law to achieve a collapse of the data, such that the point where the curve is less than 75% of the value for the perfectly wetting surfaces, the non-dimensional time equals one, $\frac{\mathcal{T}}{\tau(\theta)} = 1$.

$$\frac{\mathcal{R}}{\tau(\theta)^{\frac{1}{2}}} = \left[\frac{\mathcal{T}}{\tau(\theta)}\right]^{\frac{1}{2}} \cdot f\left(\frac{\mathcal{T}}{\tau(\theta)}\right). \tag{4.4}$$

The result of this shifting can be seen in figure 4.11. For clarity, the curve is cut at the point where it reaches 80% of the final radius, i.e. just before the capillary wave influences the behavior. We see the curves all fall on top of each other. This shows there is a common spreading behavior, independent of the contact angle. It also shows there is not a power-law behavior for which the exponent dependents on the contact angle. The contact angle only influences when the curve deviates from the $\frac{1}{2}$ power-law and what the final radius will be. If we plot the magnitude of the shift as function of the measured final contact angle, the behavior of $\tau(\theta)$ can be observed, see figure 4.12. Indeed, our data shows a nice correlation of the cross-over time with θ, justifying the assumption that the final contact angle determines the time of cross-over.
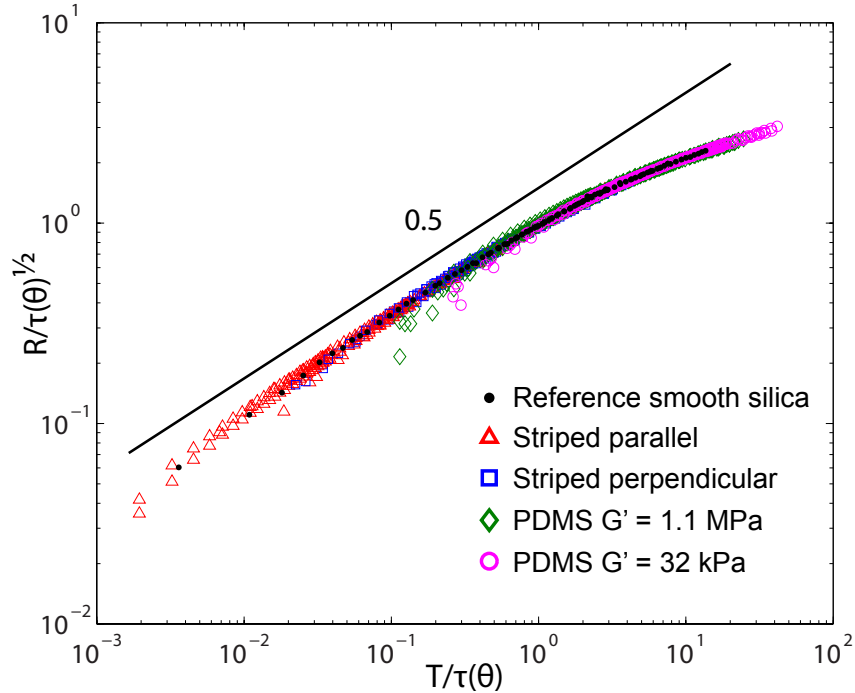

FIGURE 4.11: Collapse of all measurements on the same curve. This is achieved by shifting every measurement along the $\frac{1}{2}$ power-law. The last part of the curves (20%), where the capillary wave alters the spreading is left out for clarity.
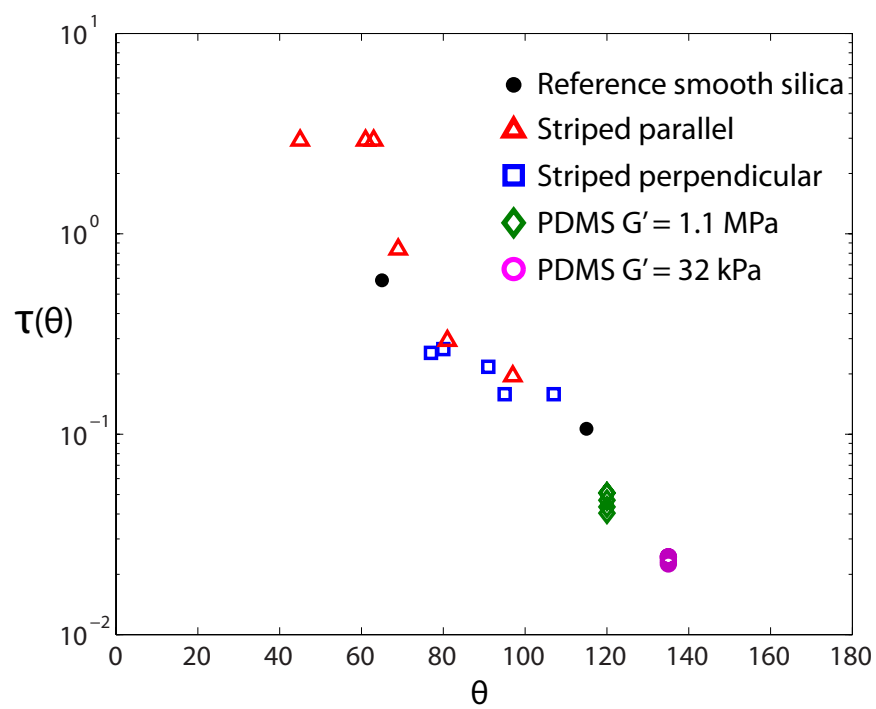
FIGURE 4.12: The applied shift $\tau(\theta)$ plotted as function of the final contact angle θ in a lin-log representation.

Chapter 5

Conclusions and Discussion

In the beginning of this thesis, we wondered if and how the surface properties are of influence on the spreading of a droplet. Especially, if the $\frac{1}{2}$ power-law behavior in the first stage of spreading ($t \lesssim 20\,\mu\text{s}$) $r \sim t^{\frac{1}{2}}$, is robust when complexity of the substrate is introduced. From the results shown, we conclude that the exponent of the power-law is not influenced by the surface properties. This was already shown for varying contact angles on smooth glass surfaces. Here is shown the roughness due to pillars does not change the initial spreading, regardless of the pillar density or size. Roughness due to chemical heterogeneity of the surface also does not change the exponent, regardless of the hydrophobic and hydrophilic surface fractions. Even for soft surfaces with $G' = 32$ kPa, $G' = 41$ kPa and $G' = 1.1$ MPa, the $\frac{1}{2}$ exponent is conserved in the initial stage of spreading. The wide variety of parameters which are probed in this research, clearly shows that there is a universal spreading dynamics for the early stage of wetting.

The explanation we propose for this universal behavior, is as follows. Due to the extreme singularity at the moment of contact, the forces driving the spreading are so violent that they are strong enough to overcast all surface effects. The only force strong enough to limit the spreading is the inertia of the liquid, the liquid cannot reach the wetted area any faster, figure 5.1. It is not shown a priori that the motion of the contact line, tangential to the surface, is not obstructed by roughness or other properties of the surface. However, all our measurements show that contact line motion is not limiting. This is supported by coalescence, where no surface effects are present because the drop spreads over its mirror image and the spreading behavior is still identical.

After the universal initial dynamics, the spreading continues until the final radius is reached. This final radius decreases for increasing final contact angle θ. If the universal dynamics would hold for larger θ, we would expect the drop to reach its final radius earlier than in the perfectly wetting case. We see however, this does not happen, the
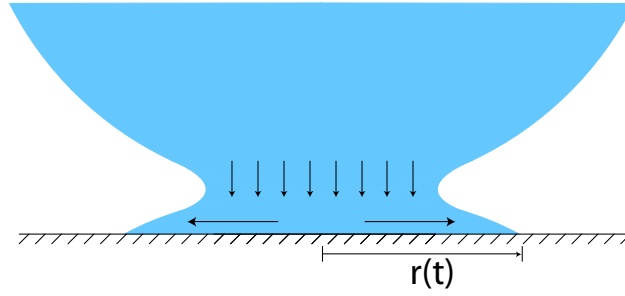
FIGURE 5.1: Limitation of the flow from the drop to the spreading contact line limits the spreading in the initial phase of spreading.

curve departs from the initial $\frac{1}{2}$ power-law and the departure starts at earlier times as the final radius is smaller. Therefore we suggest there is a cross-over time $\tau(\theta)$, which decreases for increasing final contact angle. The cross-over time is determined as the point where the value of the non-dimensional radius is less than 75% of $\mathcal{R}$ on a perfectly wetting surface. This indeed shows a decreasing behavior for increasing final contact angle, figure 4.12. When we synchronize the cross-over times, a collapse of all data on a single curve is observed, figure 4.11. Meaning that there is a universal cross-over regime between the $\frac{1}{2}$ power-law and the final radius of the wetted area. It thus follows that there is not a power-law with an exponent which depends on the contact angle in this regime, as claimed by Bird *et al.*. As this data also include experiments on viscoelastic surfaces, the theory proposed by Chen *et al.*, which includes viscoelastic effects in the exponent, is also contradicted. There is a universal cross-over regime and the only parameter needed to determine the start of this cross-over τ, is θ.

With this work we showed the spreading appears to be unaffected by other surface properties than the contact angle. When we want to test if we can break the $\frac{1}{2}$ power-law with surface properties, the effects of the surface should be increased. By lowering the shear modulus even further, the deformation might be increased enough to achieve this. Shear moduli of ~ 10 Pa can be achieved with materials like hydrogels. However, a more effective and also more convenient way is to lower the probing frequencies. As the shear modulus increases rapidly above some frequency, high probing frequencies in the initial stage will reduce the deformation making this ineffective. Therefore, lowering the probing frequency by using a liquid with much smaller surface tension, might be more convenient and might work much beter. Water with added surfactants might be such a liquid. As inertia is suggested as limiting force, it might also be interesting to see what happens if the density of the liquid is altered such that inertia becomes less important. This is probably not useful to probe the surface properties, but might result in faster spreading dynamics as inertia is not limiting the spreading anymore. However, this remains for future studies to be investigated.

Appendix A

Elasticity measurements

One of the key points in the thesis is the universal power-law behavior in the initial stage, which includes drop spreading on visco-elastic surfaces. These surfaces are characterized in this report by their shear modulus G'. Some remarks about this reported elasticity could be made but first some more information over Young's modulus and the shear modulus will be given.

The elasticity of solid materials is usually given by the Young modulus, E, defined as the tensile stress divided by the tensile strain. In spreading experiments on visco-elastic surfaces however, the shear modulus G, is much more relevant. E is related to the shear modulus as $G = \frac{E}{2(1+\nu)}$ where ν is Poisson's ratio. For incompressible visco-elastic materials, Poisson's ratio is equal to 0.5, meaning that $E = 3G$. G is a complex function which relates the strain to the stress induced by an oscillatory shear at frequency ω. The real part of G, G', represents the elastic portion of the strain, measuring the stored energy. It is in phase with the induced stress and is called the storage modulus. The imaginary part of G, G'', represents the viscous portion of the strain, measuring the as heat dissipated energy. G'' is in anti-phase with the induced stress and is called the loss modulus.

For this thesis, G' is measured by a TA Instruments DHR-3, with a stainless steel circular probe, 8 mm diameter. The probe makes an oscillatory motion to measure the shear elasticity. Because the samples are washed in THF first, they are not connected to the probe. Therefore the probe had to be pressed on the surface to measure the shear modulus. The axial force with which the probe is pressed against the sample has a large influence on the measured elasticity as can be seen in figure A.1. For the PDMS surfaces with 10:1 and 30:1 ratio between polymer and cross-linker, G' is measured with a small and large axial force. The green diamonds and magenta circles are the data where a large axial force (~ 10 N) is applied, the red squares and blue triangles are the data
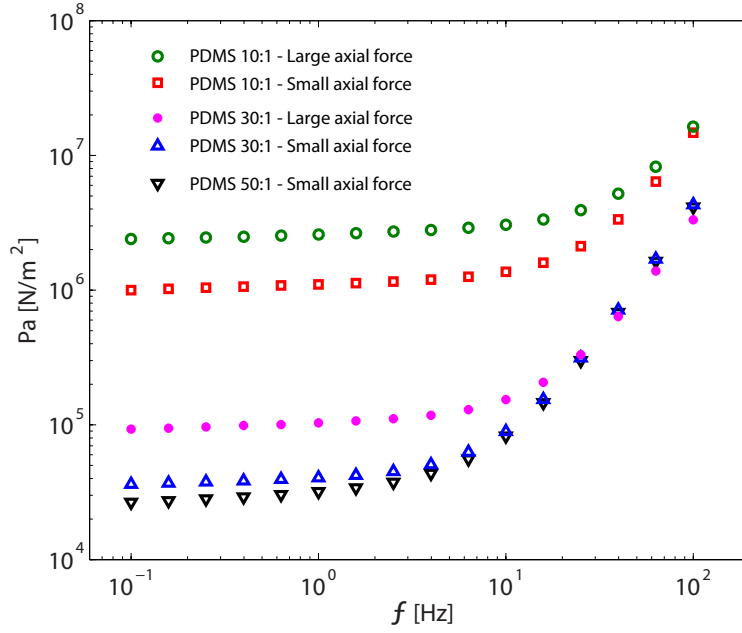
FIGURE A.1: Measurements of G' for the PDMS surfaces. The 10:1 and 30:1 mixing ratios have an additional curve measured with a large axial force. The values of three other lines measured with a small axial force at 1 Hz, are used for the characterization of the shear modulus.

where a small axial force ($\sim$ 0.1 N) is applied. The difference can clearly be observed, for large axial pressure the measured elasticity is much larger. The black up-side-down triangles correspond to the 50:1 PDMS surface measured with a small axial force.

In figure A.1, we further see that G' depends on the frequency at which it is probed. When the sample frequency f, is increased, the storage modulus G' of the visco-elastic material, will also be increased [28]. The material does not have enough time to adapt to the new situation as the deformation is not instantaneous, making it less elastic.

In the thesis, the elasticity we report is the elasticity measured with small axil force at a frequency of 1 Hz. This is closest to how the elasticity is reported in the work of Chen *et al.* although they use a different measurement technique. The question is how relevant this elasticity is for the experiment. As there is no direct frequency in drop spreading, we introduce a group which has the dimension of frequency. With the velocity of the moving contact line and the thickness of the sample as relevant parameters, we find a typical frequency when we divide the velocity by the thickness of the sample. With a typical velocity of 0.1 m/s and a thickness of 1000 μm, we find a frequency of 100 Hz. For this frequency a much larger G' ($\sim$ 2 MPa), is found from A.1. It might be argued

that the surfaces at this frequency are not soft anymore as the deformation of the surface is only $\gamma/G' \approx 40$ nm.

By varying the thickness of the sample, the frequency at which the surface is probed is changed. However, no effect of the thickness is observed in the experiments thus the deformation of the surface has no significant influence. During the spreading, the velocity of the contact line decreases. This also reduces the probing frequency, with no significant effect.

Acknowledgements

I would like to thank everyone who supported me during my study at the University of Twente. Special thanks go to Antonin Eddi, who was my daily supervisor during my Master project. He introduced me in the project and sent me in the right direction immediately. When I had a question on how to proceed, it was always helpful to discuss this with him. Also his experimental skills and French solutions to challenges in the lab helped me a lot to produce this piece of work. Without you this thesis would not be as it is now. Also Jacco Snoeijer deserves a lot of the credits as he contributed significantly to this project by suggesting directions that might and often proved to be interesting. With the interpretation of the data he was very vigorous, which led to some of the less obvious outcomes in this thesis. Both Jacco and Antonin gave me a lot of confidence and support which helped me during this project, for which I am very grateful. Further I would like to thank Devaraj van der Meer, for being chairman of my graduation committee and Detlef Lohse for giving me the opportunity to do this project here in the Physics of fluids group with all its resources. Stefan Kooij of the PIN group, I would like to thank for being in my graduation committee and his constructive advice on how to proceed with the obtained data.

I could not have done the measurements on the structured surfaces if I did not have access to these substrates. Therefore I want to thank Amy Tsai of the SFI group for giving this access. Also from the SFI group, I would like to thank Hein Verputten. He helped me with the production and washing of the soft surfaces, which took more time than I initially anticipated, without any remarks. For the work on the striped surfaces, I would like to thank Patrick Jansen from PIN. He produced these substrates and brought them to the lab where we did the experiments together.

Further I would like to thank everyone in the group for all their help and advice. Including the players of POF-United for the nice futsal games we played and my fellow students in Studentroom A, for all the nice jokes and fun at the coffee table. Thanks to you guys, I really enjoyed my time in the group, even during the less pleasant moments (although there were not much of them).

During my whole study at the university I was also supported by my friends. These include the (former) residents and acquaintances of the Bentrot, my friends from Arago, especially the BACO and friends from my secondary school. They always made sure that I could have a good time when I was not busy studying. Without you and all other friends, I never would have been able to persevere and finish the applied physics program.

As I almost thanked everyone I could think of, I would like to finish with thanking my sister Elleke, & John for their support and trust. Last but most certainly not least, I thank my parents for giving me the opportunity to follow this education and all the other things they did to support me whenever I needed it.

Bram Stapelbroek, June 28th 2013

Bibliography

[1] Martin Rein. Drop-surface interaction. 2002.

[2] David Quéré. Leidenfrost dynamics. *Annual Reviews*, 45:197–215, 2013. doi: 10. 1146/annurev-fluid-011212-140709.

[3] P Tabeling. Introduction to microfluidics. 2005.

[4] Shahidzadeh N., Bertrand E., Dauplait J.P., Borgotti J.C., Vie P., and Bonn D. Effect of wetting on gravity drainage in porous media. *Transport in Porous Media*, 52(2):213–227, 2003.

[5] T Young. An essay on the cohesion of fluids. *Philosophical Transactions*, 95:65–87, 1805.

[6] A. Pockels. Surface tension. *Nature*, 43:437439, 1891. doi: 10.1038/043437c0.

[7] Antonin Marchand, Joost H Weijs, Jacco H Snoeijer, and Bruno Andreotti. Why is surface tension a force parallel to the interface? *American Journal of Physics*, 79:999, 2011.

[8] P. G. De Gennes. Wetting: statics and dynamics. *Rev. Mod. Phys.*, 57:827–863, Jul 1985. doi: 10.1103/RevModPhys.57.827.

[9] Daniel Bonn, Jens Eggers, Joseph Indekeu, Jacques Meunier, and Etienne Rolley. Wetting and spreading. *Reviews of Modern Physics*, 81(2):739–805, May 2009. doi: 10.1103/revmodphys.81.739.

[10] J.H. Snoeijer and B. Andreotti. Moving contact lines: Scales, regimes, and dynamical transitions. *Annual review of fluid mechanics*, 45:269 – 292, 2013.

[11] L. H. Tanner. The spreading of silicone oil drops on horizontal surfaces. *Journal of Physics D Applied Physics*, 12:1473–1484, September 1979. doi: 10.1088/ 0022-3727/12/9/009.

[12] Anne-Laure Biance, Christophe Clanet, and David Quéré. First steps in the spreading of a liquid droplet. *Phys. Rev. E*, 69:016301, Jan 2004. doi: 10.1103/PhysRevE. 69.016301.

[13] J. Eggers, J. R. Lister, and H. A. Stone. Coalescence of liquid drops. *Journal of Fluid Mechanics*, 401:293–310, 1999.

[14] James C. Bird, Shreyas Mandre, and Howard A. Stone. Short-time dynamics of partial wetting. *Phys. Rev. Lett.*, 100:234501, Jun 2008. doi: 10.1103/PhysRevLett. 100.234501.

[15] Koen G. Winkels, Joost H. Weijs, Antonin Eddi, and Jacco H. Snoeijer. Initial spreading of low-viscosity drops on partially wetting surfaces. *Phys. Rev. E*, 85: 055301, May 2012. doi: 10.1103/PhysRevE.85.055301.

[16] A. Eddi, K.G. Winkels, and J.H. Snoeijer. Short time dynamics of viscous drop spreading. *Physics of Fluids*, 25(1), 2013. doi: 10.1063/1.4788693.

[17] C. Pirat, M. Sbragaglia, A.M. Peters, B.M. Borkent, R.G.H. Lammertink, M. Wessling, and D. Lohse. Multiple time scale dynamics in the breakdown of superhydrophobicity. *Europhysics Letters*, 81(6):66002, 2008.

[18] Olesya Bliznyuk, H. Patrick Jansen, E. Stefan Kooij, and Bene Poelsema. Initial spreading kinetics of high-viscosity droplets on anisotropic surfaces. *Langmuir*, 26 (9):6328–6334, 2010.

[19] Marcus C. Lopes and Elmar Bonaccurso. Evaporation control of sessile water drops by soft viscoelastic surfaces. *Soft Matter*, 8(30):3875, 2012.

[20] Alain Carré, Jean-Claude Gastel, and Martin E. R. Shanahan. Viscoelastic effects in the spreading of liquids. *Nature*, 379(6564):432–434, February 1996. doi: 10. 1038/379432a0.

[21] P. G. De Gennes, F. Brochard-Wyart, D. Quéré, A. Reisinger, and B. Widom. Capillarity and Wetting Phenomena: Drops, Bubbles, Pearls, Waves. 2004.

[22] David Quere. Surface chemistry: Fakir droplets. *Nature Materials*.

[23] Zen Yoshimitsu, Akira Nakajima, Toshiya Watanabe, and Kazuhito Hashimoto. Effects of surface structure on the hydrophobicity and sliding behavior of water droplets. *Langmuir*, 18(15):5818–5822, 2002. doi: 10.1021/la020088p.

[24] Robert N. Wenzel. Resistance of solid surfaces to wetting by water. *Industrial and Engineering Chemistry*, 1936. doi: 10.1021/ie50320a024.

[25] O. Bliznyuk, E. Vereshchagina, E. Stefan Kooij, and Bene Poelsema. Scaling of anisotropic droplet shapes on chemically stripe-patterned surfaces. *Phys. Rev. E*, 79:041601, Apr 2009. doi: 10.1103/PhysRevE.79.041601.

[26] H.P. Jansen, K. Sotthewes, C. Ganser, C. Teichert, H.J.W. Zandvliet, and E.S. Kooij. Tuning kinetics to control droplet shapes on chemically stripe patterned surfaces. *Langmuir*, 2012.

[27] Tadashi Kajiya, Adrian Daerr, Tetsuharu Narita, Laurent Royon, Francois Lequeux, and Laurent Limat. Advancing liquid contact line on visco-elastic gel substrates: stick-slip vs. continuous motions. *Soft Matter*, 9:454–461, 2013. doi: 10.1039/C2SM26714D.

[28] J.D. Ferry. Viscoelastic properties of polymers. 1980.

[29] L. Q. Chen, G. K. Auernhammer, and E. Bonaccurso. Short time wetting dynamics on soft surfaces. *Soft Matter*, 7:9084, 2011.

[30] Longquan Chen, Elmar Bonaccurso, and Martin E. R. Shanahan. Inertial to viscoelastic transition in early drop spreading on soft surfaces. *Langmuir*, 29(6):1893, 2013.

[31] A. Marchand. Mouillage statique et dynamique: Influences géométriques aux échelles moléculaires.

[32] Mauro Sbragaglia, Alisia M. Peters, Christophe Pirat, Bram M. Borkent, Rob G. H. Lammertink, Matthias Wessling, and Detlef Lohse. Spontaneous breakdown of superhydrophobicity. *Phys. Rev. Lett.*, 99:156001, Oct 2007. doi: 10.1103/PhysRevLett.99.156001.

[33] M. E. R. Shanahan and A. Carré. Viscoelastic Dissipation in Wetting and Adhesion Phenomena. *Langmuir*, 11(4):1396–1402, April 1995. doi: 10.1021/la00004a055.